AIAA JOURNAL
Vol. 45, No. 3, March 2007

Numerical Parametric Analysis of Dual-Bell Nozzle Flows

Emanuele Martelli,* Francesco Nasuti,† and Marcello Onofri‡
University of Rome "La Sapienza," 00184 Rome, Italy

DOI: 10.2514/1.26690

Dual-bell nozzles permit two different operating modes, which provide higher performance than conventional bell nozzles when applied to rocket engines operating from sea level. During the low-altitude mode, the flow is separated and the separation line is located near the inflection of the nozzle wall, in a region characterized by a negative value of the wall pressure gradient, as in conventional nozzles, and in which side loads may occur. The characteristics of this region in hot full-scale applications are addressed by means of numerical simulations, and scaling laws are sought for cold subscale side-load experiments. Moreover, the flow behavior during the transition between the two operating modes is analyzed by time-accurate simulations.

Nomenclature

$\mathcal{A}$	=	cross-sectional area
A	=	wall position at which $\pi_{\xi,A} = 0.1\pi_{\xi,i}$
a	=	speed of sound
B	=	wall position at which $\pi_{\xi,B} = 0$
$\mathcal{F}$	=	functional dependency
F_{sl}	=	side force
g	=	gravity constant
K_{sl}	=	constant value in Schmucker's side-load formula
l	=	length
M	=	Mach number
PR	=	pressure ratio, p_c/p_a
p	=	pressure
R	=	gas constant
Re	=	Reynolds number
r	=	radius
T	=	temperature
t	=	time
u	=	flow velocity
V	=	launcher velocity
x	=	abscissa
z	=	altitude
α	=	change of wall angle at the inflection
γ	=	gas specific heat ratio
δ	=	nondimensional boundary-layer thickness
ϵ	=	area ratio, $\mathcal{A}/\mathcal{A}_t$
λ	=	nondimensional axial distance, l/r_t
μ	=	viscosity
ξ	=	nondimensional abscissa, x/r_t
π	=	nondimensional pressure, p/p_c
π_ξ	=	nondimensional wall pressure gradient, $\mathrm{d}\pi/\mathrm{d}\xi$
ρ	=	density
τ	=	nondimensional time, $t/(r_t a_c)$
τ_{sl}	=	nondimensional side-load time, $t_{\mathrm{sl}} \cdot gV/(R_a T_a)$
Φ_{sl}	=	nondimensional side-load force, $F_{\mathrm{sl}}/(K_{\mathrm{sl}} p_c \mathcal{A}_t)$

Subscripts

A, B	=	relevant to operation with the separation point in A and B
a	=	ambient
b	=	base, value at the end of the base
c	=	combustion chamber
e	=	extension
i	=	inflection region
min	=	minimum value
o	=	overall nozzle
s	=	separation point
t	=	throat
tr	=	transition
0	=	sea-level value, initial value

I. Introduction

THE introduction of new-generation nozzles is one of the possible ways to increase the engine performance and, thus, the launcher payload mass fraction. The advanced nozzle concept discussed in the present study is the dual-bell nozzle, which can be considered as a possible compromise between revolutionary and conventional nozzle shapes [1,2]. The existence of a discontinuity in the nozzle contour defines the peculiar dual-bell shape, dividing the divergent section into an upstream part, *the base*, and a downstream part, *the extension*; in particular, from one side, this shape permits the larger expansion ratio that is required for a more efficient nozzle at high altitude, and from the other side, it forces the separation line position at the inflection in the highly overexpanded condition that takes place at sea level (Fig. 1). Therefore, the dual-bell nozzle features two different operating modes, relevant to two different design altitudes. In the low-altitude operating mode (OM1), the flow is attached in the base and separated downstream of the inflection (Fig. 2a). In this case, the separation point is placed in a precise location, at the inflection, and thus a symmetrical separation takes place that guarantees a low level of side loads. At high altitude (OM2), the nozzle operates with attached flow in the whole divergent section (Fig. 2b). Therefore, the limitation of nozzle expansion ratio due to the avoidance of unsymmetrical flow separation at sea level can be circumvented, and, consequently, higher vacuum specific impulse can be obtained (compared with classical bell nozzles, which display a single design altitude). The main advantage of a dual-bell nozzle is that this increased vacuum performance is obtained without adding heavy moving parts to the engine.

Nevertheless, numerical [3] and experimental [4,5] studies seem to indicate that side loads increase, with respect to OM2, in the proximity of the OM1/OM2 transition. Although the side-load level is quite lower than in the separated flow operation of conventional nozzles, a deeper investigation on the causes for these side loads is useful for a better understanding of dual-bell nozzle flow and operations. To this goal, it has to be remembered that in the ideal case, the discontinuity between the two bells causes a step in the wall

Received 24 July 2006; accepted for publication 15 December 2006.

*Research Fellow, Department of Mechanics and Aeronautics, via Eudossiana 18. Member AIAA.
†Associate Professor, Department of Mechanics and Aeronautics, via Eudossiana 18. Senior Member AIAA.
‡Professor, Department of Mechanics and Aeronautics, via Eudossiana 18. Senior Member AIAA.

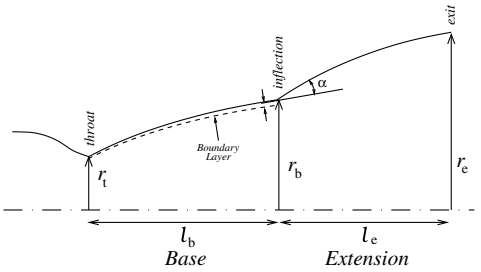

Fig. 1 Schematic of a dual-bell nozzle.

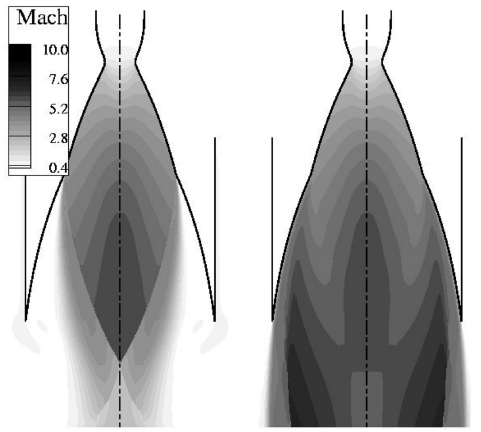

a) OM1 **b) OM2**

Fig. 2 The two main operating modes of a dual-bell nozzle.

pressure behavior; thus, during OM1, the separation point would be anchored at the discontinuity, avoiding the onset of side loads. In the real case, the viscosity effects transform the ideal step into a region of finite length, in which the pressure gradient is negative, such as in a conventional nozzle. In this region (which will be referred to as the *inflection region)*, the separation point finds stable, but not symmetric, equilibrium positions (because of the inevitable flow asymmetries), and thus side loads may occur, such as in the case of a conventional bell nozzle.

Aiming to explore in detail the phenomena that may lead to the generation of side loads in dual-bell nozzles, the present study analyzes the geometrical and physical parameters that affect the flow in the inflection region. Moreover, the role of real gas properties is studied to find how to scale the results from cold subscale models to hot full-scale applications. After functional dependencies are inferred by theoretical considerations, their relative importance is quantified by means of a validated multispecies turbulent Navier–Stokes solver, together with empirical criteria for flow separation and side-load prediction. Note that these criteria lack accuracy in the prediction of the exact value of the separation-point location and the side-load intensity. Nevertheless, it can be assumed that they provide the reasonable functional dependencies, and thus they are suitable for a comparative analysis of different nozzles. To complete the analysis of the possible causes that may generate side loads in dual-bell nozzles, time-accurate simulations of the transition from OM1 to OM2 are carried out for three nozzles having different inflection regions.

The numerical parametric analysis is made by introducing suitable nondimensional variables. For the sake of compactness, each nondimensional value is indicated by the Greek letter (λ, Φ, π, τ, and ξ) corresponding to the Latin letter commonly used for the variable (l, F, p, t, and x).

II. Dual-Bell Nozzle Flows

A. Basic Features

Dual-bell nozzle geometry has to be designed to provide good performance during both OM1 and OM2, while being able to safely

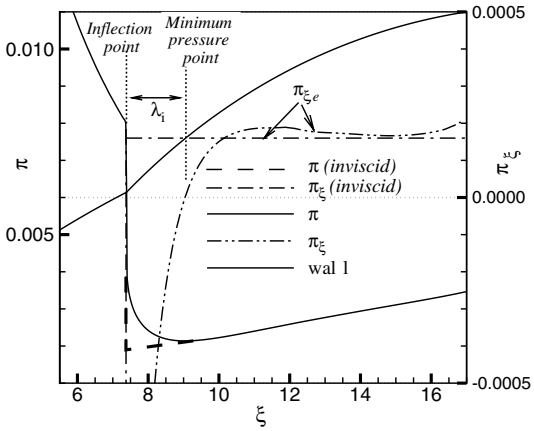

Fig. 3 Wall pressure behavior in the extension of a LIP dual-bell nozzle and definition of the inflection region. Plots are relevant to a cold subscale model [20].

operate with separated flow inside the nozzle during OM1. The basic features of this nozzle are thus summarized by the two area ratios, the length and shape of the base, and the length and shape of the extension profile. The choice of the shape of the extension profile governs not only performance, but also the transition behavior of the nozzle. A trade-off must be made, because the safest is also the worst-performing profile [6]. In particular, it has been shown that to have a sudden transition between OM1 and OM2 (and thus a different behavior with respect to a conventional nozzle), the wall pressure gradient in the extension (during attached-flow operations, that is, OM2) must be positive, or at least zero ($\pi_{\xi,e} \geq 0$) [6]. Because the latter is the limiting value, a positive gradient has been selected in the following analysis and, to narrow the number of possible cases, attention will only be focused on extensions showing a constant wall pressure gradient ($\pi_{\xi,e}$ is constant); they will be referred to as linearly increasing wall pressure (LIP) dual-bell nozzles.

Typical wall pressure and wall pressure gradient behavior in a LIP dual-bell nozzle are shown in Fig. 3. At the geometrical discontinuity, there is a sudden wall pressure drop and then wall pressure slightly increases in the extension. The wall pressure gradient passes from a finite negative value in the base to an infinite negative value at the geometrical discontinuity, and it finally reaches a constant positive value in the extension. With more realistic assumptions, the behavior changes. In particular, viscous effects make the pressure gradient a finite value also at the geometrical discontinuity. The value varies from high (finite) negative values to zero and then it becomes positive, forced by the considered LIP shape.

The positive gradient region, in which the separation point is expected to assume stable positions neither during OM1 nor during transition [6], begins at the minimum pressure point and not at the geometrical discontinuity. Therefore, during OM1, the separation point, rather than being placed exactly at the geometrical discontinuity, can move in a region of negative wall pressure gradient, such as in conventional nozzles. This region (Fig. 3) has been referred to as the inflection region [6] and its dimension (the inflection region length $\lambda_i = l_i/r_t$) is defined as the region from the geometrical discontinuity to the minimum pressure point. The values of the inflection region length, and of the wall pressure gradient occurring inside it, are the key parameters to evaluate the expected level of side loads during OM1.

B. Side Loads

The generation of side loads in conventional overexpanded nozzles has been extensively studied. In particular, according to Schmucker [7] the side load can be modeled by a bias of the separation line from its averaged symmetric position. The resulting side load F_{sl}, due to an unsymmetrical separated area, is evaluated as

$$F_{\mathrm{sl}} = K_{\mathrm{sl}} p_c \mathcal{A}_t \left(\frac{r_s}{r_t}\right) \frac{\mathcal{F}_1(M_s, \gamma)}{|\pi_{\xi,s}|} \tag{1}$$

where $\pi_{\xi,s}$ is the nondimensional attached-flow wall pressure gradient at separation-point abscissa; r_s is the average nozzle radius at the separation point; K_{sl} is a nondimensional constant for which the value, in the case of conventional nozzles, can be obtained by those of constants introduced in [7]; and $\mathcal{F}_1$ is a nondimensional expression depending on the flow Mach number and γ outside of the boundary layer at the separation point. Assuming constant gas specific heat ratio through the nozzle, $\mathcal{F}_1$ can be expressed as

$$\mathcal{F}_1(M_s, \gamma) = \frac{[1 + 0.5(\gamma-1)M_s^2]^{-\frac{2\gamma}{\gamma-1}}[(1.88M_s - 1)^{0.64} - 1]}{1 - 1.2032[1 + 0.5(\gamma-1)M_s^2][\gamma M_s(1.88M_s - 1)]^{-1}} \tag{2}$$

It is worth remembering that Eq. (1) is only valid when $\pi_\xi < 0$ and provides an empirical law for the prediction of side loads when the separation point is placed at a specific wall position (featuring a value of M_s, π_s, and $\pi_{\xi,s}$) because of the specific ambient pressure and chamber pressure values.

The application of Eq. (1) is straightforward for conventional nozzles, whereas it must be more carefully considered in the case of dual-bell nozzles, in which the values outside the boundary layer of the attached-flow viscous solution should be considered as input for Eq. (1), rather than the inviscid solution. In fact, if ambient pressure is low enough to show attached flow in the base, the inviscid dual-bell nozzle solution predicts that separation can only be placed at the inflection for which $\pi_\xi \to -\infty$, because π_ξ is positive in the extension. Thus, on the basis of Eq. (1), no side load should be expected. On the contrary, if the values outside the boundary layer of the viscous solution with attached flow are considered, the side-load strength is determined by the actual finite value of $|\pi_\xi|$ in the finite inflection region, for which π_ξ is negative.

To better clarify why attention has to be paid to the onset of side loads during OM1, it is useful to make a gross estimation of the time spent with the separation point in the inflection region during a typical launcher ascent. To this goal, a hot full-scale dual-bell nozzle with a truncated ideal contour nozzle (TIC)-shaped base, and having the properties reported in Table 1, has been considered. The area ratios of the base and the extension have been chosen according to [8]. From the computed wall pressure profile shown in Fig. 4, it can be seen that the inflection region can be divided into two zones: the first one ranges from the inflection point to the location at which the wall pressure gradient modulus is, say, 10% of its maximum value (point A in Fig. 4); the second one, nearly two-throat-diameters long, ranges from point A to point B, which indicates the location at which the pressure gradient is null (minimum wall pressure point). In the first zone, the wall pressure gradient is very high and, thus, the expected side-load level is very low. Conversely, in the AB region, a higher level of side loads is expected, as can easily be understood by considering the lower average value of the wall pressure gradient.

Table 1 Geometric and combustion chamber operating conditions of the reference full-scale dual-bell nozzle

Throat radius r_t, m	0.1
Chamber temperature T_c, K	3500
Chamber pressure p_c, MPa	12
Nondimensional base length λ_b	16.6
Nondimensional extension length λ_e	14.3
Nondimensional divergent section length λ_o	30.9
Base area ratio ϵ_b	48
Overall area ratio ϵ_o	115
Oxidizer to fuel mass ratio O/F	6
Average (1-D) Mach number at base exit $\bar{M}_b$	4.45
Ratio of specific heats γ_c, $\bar{\gamma}_b$	1.19, 1.26
Inflection angle α	13.68 deg
Chamber Reynolds number $Re_c = \rho_c a_c r_t/\mu_c$	$1.044 \cdot 10^7$
Nondimensional extension-design wall pressure gradient $\pi_{\xi,e}$	$3 \cdot 10^{-5}$

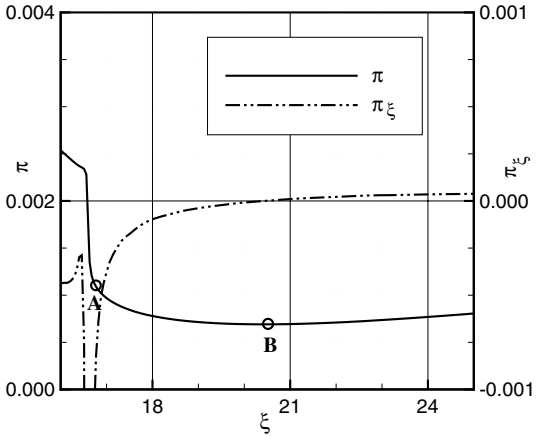

Fig. 4 Wall pressure and its gradient for a full-scale dual-bell nozzle; enlargement of the inflection region.

The time interval during which the separation point lies between the points A and B, indicating the duration of operation with OM1 side loads, can be computed following the approach of [9]. The critical time interval is given by the launch phase for which the separation wall pressure is between $p_s = p_A$ and $p_s = p_B$, where p_A and p_B are the values, indicated in Fig. 4, that depend on p_c. The values p_A and p_B can be translated into the corresponding ambient pressure values $p_{a,A}$ and $p_{a,B}$, by the separation criterion of Schmucker [10]. For the present dual bell (Table 1) $p_A = 13637$ Pa, which corresponds to the ambient pressure $p_{a,A} = 49612$ Pa and to the altitude $z_A = 5632$ m, whereas $p_B = 8290$ Pa corresponds to $p_{a,B} = 31471$ Pa and $z_B = 8843$ m. The typical time spent by existing launchers within this range of altitudes is $t_{A-B} \approx 11$ s. This is quite a long time and, therefore, it is mandatory to be able to predict the level of side loads that could appear in this time interval, by both numerical and experimental investigations. Although this time could be reduced by throttling, it should be noted that for the present nozzle, a variation of chamber pressure of approximately 60 bar would be necessary.

III. Similarity Rules

The preceding considerations on side loads in dual-bell nozzles indicate that OM1 could be critical because of the existence of a finite length inflection region. For this reason, the inflection region is studied considering the geometric and flow parameters affecting its dimension and the side-load intensity. To individuate the influence parameters, it can be easily recognized that the flow in the inflection region depends on the wall boundary-layer thickness at the end of the base, on the Prandtl–Meyer expansion at the inflection, and on the kind and intensity of the pressure gradient in the extension $\pi_{\xi,e}$.

The nondimensional boundary-layer thickness δ for incompressible turbulent flows on a flat plate [11] is

$$\delta = 0.37 \frac{x}{L} \left(\frac{\rho u x}{\mu}\right)^{-0.2} \tag{3}$$

where the origin of abscissas x is at the plate leading edge; ρ, u, and μ are local density, velocity, and viscosity outside the boundary layer, respectively; and L is a reference length. A general power law cannot be obtained for compressible flows. However, for the purpose of the present analysis, it is sufficient to remember that

$$\delta = \mathcal{F}_2\left(\frac{x}{L}, \frac{\rho u x}{\mu}, M\right) \tag{4}$$

where the dependency on Mach number outside the boundary layer has been added with respect to the incompressible case. Assuming zero thickness at the throat (as can reasonably be made for supersonic nozzles [12]), the nondimensional boundary-layer thickness at the beginning of the inflection region (that is, at the exit of the base) can be expressed as

$$\delta_b = \mathcal{F}_3\left(\frac{l_b}{r_t}, \frac{\rho_b u_b l_b}{\mu_b}, M_b\right) \tag{5}$$

where the subscript b indicates wall values at the end of the base. The local Reynolds number in Eq. (5) can be expressed as a function of a reference Reynolds number Re_c, based on the throat radius and combustion chamber density, temperature, and speed of sound. Using the perfect gas equation of state and the definition of the speed of sound, the reference nozzle Reynolds number can be written as

$$Re_c = \frac{\rho_c a_c r_t}{\mu(T_c)} = \frac{p_c r_t}{\sqrt{R_c T_c}} \frac{\sqrt{\gamma_c}}{\mu(T_c)} \tag{6}$$

and inserting Eq. (6) in the term with the local Reynolds number of Eq. (5)

$$Re_b = \left(\frac{\rho_b u_b l_b}{\mu(T_b)}\right) = \left(\frac{\rho_c a_c r_t}{\mu(T_c)}\right)\left[M_b\left(\frac{\rho_b}{\rho_c}\right)\left(\frac{a_b}{a_c}\right)\left(\frac{\mu(T_c)}{\mu(T_b)}\right)\right]\left(\frac{l_b}{r_t}\right) \tag{7}$$

The bracketed term is a product of M_b and ratios of thermodynamic variables in the chamber and at the base exit. These ratios depend essentially on average γ and on M_b (it is a simple function of M_b and γ for constant-γ flows), because the ratio μ_b/μ_c can be roughly expressed as a power of the ratio T_b/T_c. It is then possible to express Re_b by a function $\mathcal{F}_4$ of the local Mach number and average γ (which, in turn, can be considered as a function of its local value at the base exit γ_b):

$$Re_b = \lambda_b Re_c \mathcal{F}_4(M_b, \gamma_b) \tag{8}$$

As a consequence of Eqs. (5) and (8), the boundary-layer thickness at the inflection region can be finally written as

$$\delta_b = \mathcal{F}_3(\lambda_b, Re_b, M_b) = \mathcal{F}_5(\lambda_b, Re_c, M_b, \gamma_b) \tag{9}$$

Note that although the subscript $(\,)_b$ indicates the variables evaluated just outside the boundary layer (that is, the *inviscid wall values*) at the end of the base, they can easily be replaced by 1-D inviscid values, considering that the wall values of M_b and γ_b depend on the average 1-D base exit values $\bar{M}_b$ and $\bar{\gamma}_b$ and on the base length λ_b, once the shape of the base profile is selected (TIC nozzle, in the present case). Therefore,

$$\delta_b = \mathcal{F}_6(\lambda_b, Re_c, \bar{M}_b, \bar{\gamma}_b) \tag{10}$$

A second phenomenon affecting the dimension of the inflection region is the centered expansion generated by the convex corner. In particular, following the Prandtl–Meyer theory for stationary supersonic flows of perfect gases across the expansion fan the compatibility equation along the characteristic line C^+ holds, and therefore the expansion fan and the flow conditions downstream of the corner can be expressed as a function of the upstream Mach number M_b, the change of wall slope α (see Fig. 1), and the specific heat ratio γ_b. For the same preceding considerations, the flow conditions downstream of the corner can be expressed as a function of $\bar{M}_b$, $\bar{\gamma}_b$, α, and λ_b.

Besides the development of corner expansion, the dimension of the inflection region is determined by the pressure gradient enforced by the extension shape. In fact, this is the driving force to obtain a change of pressure gradient sign. In practice, the recompression waves generated from the LIP extension interact with the expansion fan originating from inflection, and the effect of this interaction is to determine the position of the minimum pressure point. The effect obviously depends on the design value of the wall pressure gradient of the extension, which is therefore a further key parameter affecting the length of the inflection region.

Summarizing the nondimensional length of the inflection region depends on the following parameters: 1) δ_b, the nondimensional boundary-layer thickness at the end of the base; 2) λ_b, the nondimensional length of the base; 3) $\bar{M}_b$, the inviscid 1-D Mach number at the end of the base; 4) $\bar{\gamma}_b$, the gas specific heat ratio; 5) α, the angle of the inflection point, relative to the base wall exit angle; and 6) $\pi_{\xi,e}$, the nondimensional value of the extension-design wall pressure gradient.

Therefore, it can be written

$$\lambda_i = \mathcal{F}_7(\delta_b, \lambda_b, \bar{M}_b, \bar{\gamma}_b, \alpha, \pi_{\xi,e}) \tag{11}$$

Considering Eqs. (10) and (11), the nondimensional length of the inflection region can be finally written as

$$\lambda_i = \mathcal{F}_8(\lambda_b, Re_c, \bar{M}_b, \bar{\gamma}_b, \alpha, \pi_{\xi,e}) \tag{12}$$

The study of λ_i allows one to obtain a rough estimate of critical operation during OM1. However, the evaluation of the role of the inflection region on the intensity of side loads needs an evaluation of Eq. (1). This can be made by introducing the nondimensional side load $\Phi_{sl} = F_{sl}/(K_{sl} p_c \mathcal{A}_t)$, which depends on $|\pi_\xi|$ and, thus, on the development of the inflection region and, thus, on the same variables as λ_i. Therefore, a relationship such as Eq. (12) can also be written for Φ_{sl}. In the following discussion, the effects of the basic parameters on the inflection region length and side loads are addressed. Then scaling considerations are done to reproduce the same inflection region in a cold subscale and in a hot full-scale application.

IV. Numerical Analysis of Flow Scaling

The analysis of a dual-bell nozzle flowfield is performed by a 2-D axisymmetric time-accurate multispecies reacting Reynolds-averaged Navier–Stokes solver, based on the approach described in [13,14]. The main features of this method are to discretize the convective terms according to the lambda scheme and to handle shock discontinuities by a fitting technique [15,16]. The viscosity and conductivity of the single species are described by Sutherland's law, and the mixture properties are derived from Wilke's rule. The diffusion coefficient is obtained assuming constant Lewis number. Turbulence is computed by a modified version [17] of the Spalart–Allmaras [18] one-equation model, which takes into account the compressibility effects.

Only flows without separation inside the nozzle are considered; therefore, the computational domain is defined by the nozzle geometry, with subsonic inflow boundary conditions describing combustion chamber (total temperature and total pressure are enforced together with the flow direction), supersonic outflow, symmetry axis, and adiabatic wall.

The common feature of all dual-bell nozzles considered in the following is that they are designed with a LIP extension. This means that two parameters unambiguously define the extension for the assigned extension expansion ratio [6]. In particular, once the inflection angle α and the extension pressure gradient $\pi_{\xi,e}$ are selected, the extension length λ_e is unambiguously determined. The reference geometry is the hot full-scale dual-bell nozzle displaying the main characteristics reported in Table 1. The nozzle gas is a mixture of water and hydrogen, for which concentrations come from the complete combustion of oxygen and hydrogen. The flow in the nozzle is considered in vibrational equilibrium and chemically frozen (γ of the mixture varies because of temperature variations). The dependence of the inflection region, and of the flow behavior when the separation point lies in this region, on the different parameters shown in Eq. (12) is studied in the following, with the exception of $\bar{M}_b$. In fact, $\bar{M}_b$ is directly connected to ϵ_b, which is considered as an assigned design parameter. The nozzle profiles are designed by the method of characteristics, as illustrated in [6].

A. Influence of the Wall Inflection Angle

Three nozzles have been designed, starting from the reference nozzle (Table 1), by changing the wall angle α, while keeping all other parameters constant. The overall nozzle length λ_o and extension expansion ratio ϵ_o could be chosen arbitrarily as attention is focused on the inflection region. However, in the present study, as the value of ϵ_o is prescribed, the value of λ_o is computed according to the values of ϵ_o and α. Because properties of the base are equal in all

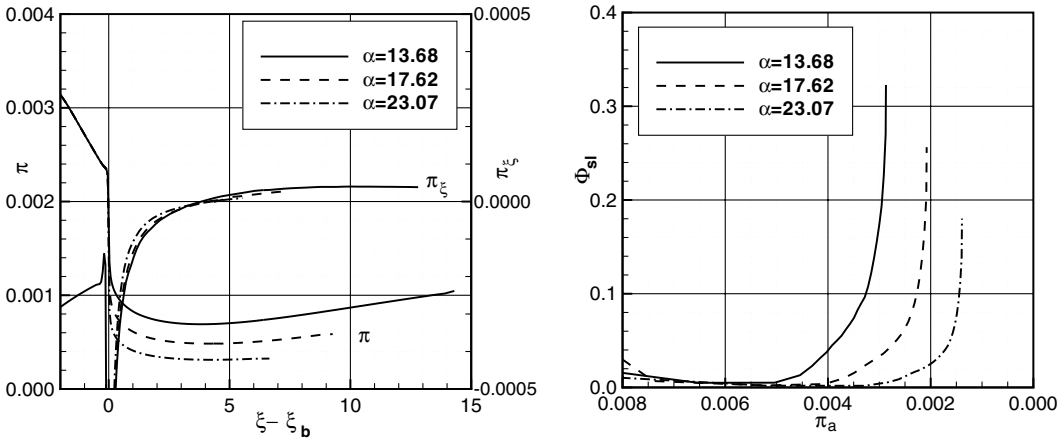

a) Wall pressure in the inflection region **b) Side loads for varying ambient pressure**

Fig. 5 Effect of the inflection angle on the wall pressure behavior, inflection region length, and side loads.

the cases, the wall boundary-layer thickness at the end of the base is the same and, also keeping constant $\pi_{\xi,e}$, the only parameter left free to vary in Eq. (12) is α. The effect of varying α is described by Fig. 5a, in which the wall pressure is displayed, along with its gradient as a function of the distance from the inflection point. Increasing α, the flow expands more, the value of the minimum wall pressure $p_{\min}$ decreases, and its location shifts downstream, thus slightly enlarging the inflection region, as can be seen in Table 2, in which the values of the assigned parameters are reported, together with the resulting properties of the inflection region. The reported properties are the ratio $p_b/p_{\min}$ (indicating the expansion ratio of the inflection region); the length of the inflection region λ_i (from the base exit pressure to the pressure minimum location); the maximum side-load value $\Phi_{sl,max}$ [computed by Eq. (1), with separation placed in the point at which wall pressure is 5% higher than minimum (this pressure value is taken by typical range of chamber pressure fluctuations considered in Schmucker's side-load formula [7])]; and the duration of large OM1 side loads τ_{sl}. The last value is computed considering the range of ambient pressure for which Φ_{sl} is greater than a threshold value (say, 0.02), and its nondimensional value for an assigned chamber pressure is given by

$$\Delta\pi_a = \pi_{a,1} - \pi_{a,2} \quad \text{with}$$
$$\begin{cases} \pi_{a,1} & = \text{value of } \pi_a \text{ when } \Phi_{sl} = 0.02 \\ \pi_{a,2} & = \text{value of } \pi_a \text{ when } \Phi_{sl} = \Phi_{sl,max} \end{cases} \tag{13}$$

From this relationship and the hypotheses of isothermal atmosphere and constant launch vehicle velocity in the present range of ambient pressure, the duration of operation with side loads larger than the threshold value can be computed as

$$\tau_{sl} = \frac{t_{sl}}{(R_a T_a)/(gV)} = -\ell n\left(1 - \frac{\Delta\pi_a}{\pi_{a,1}}\right) \tag{14}$$

The behavior of nondimensional side load Φ_{sl} as a function of the nondimensional ambient pressure π_a is shown in Fig. 5b. Table 2 shows that increasing the wall angle by a factor of 70% causes an 11% increase of the inflection region length, thus indicating a low sensitivity of λ_i to the wall inflection angle. A more important effect on the side loads is caused by the variation of wall pressure gradient π_ξ. It can be seen from Fig. 5a that increasing α decreases the module of the wall pressure gradient in the first part of the inflection region, whereas increasing values are found at the vicinity of the minimum pressure point. This has a positive effect: according to Eq. (1), the maximum side-load value decreases (Fig. 5b), whereas OM1 side-load duration shows a nonmonotonic behavior. It has to be underlined that the variation of τ_{sl} is rather small.

B. Influence of the Wall Pressure Gradient

The effect of the wall pressure gradient is analyzed by considering increasing values of $\pi_{\xi,e}$, starting again from the reference nozzle of Table 1. From Fig. 6, it can be seen that the effect of increasing the pressure gradient is to reduce λ_i and that the effect on λ_i is much more visible than that in the case of varying α. Besides a λ_i reduction, increasing $\pi_{\xi,e}$ generates a steeper curve of π_ξ, indicating an increase of average $|\pi_\xi|$. The result is a twofold positive effect of $\pi_{\xi,e}$ increase on OM1 side loads: $\Phi_{sl,max}$ decreases and τ_{sl} decreases (see Table 3). The result can be thus summarized by stating that there is a high sensitivity of the inflection region length to the wall pressure gradient: increasing the former yields a reduction of the latter. However, it should be also considered that there is a trade-off with performance: the higher $\pi_{\xi,e}$, the lower the nozzle vacuum performance [6].

C. Influence of the Base Length

The relative length of the base directly influences the boundary-layer thickness at the beginning of the inflection region, as shown by Eq. (5). Two more nozzles are designed with a shorter value of λ_b with respect to the reference nozzle (Table 4). Figure 7 shows that the wall pressure at the inflection increases as the base length is shortened; as a consequence, the ratio of inflection point to minimum base pressure increases. The behavior of wall pressure and wall pressure gradient is not changed significantly by the length of the base. As a consequence, a modest effect is found on side loads and on their duration at a significant level. In particular, λ_b reduction leads to a slight $\Phi_{sl,max}$ reduction, whereas τ_{sl} remains practically unchanged. It is worth stressing that the reduction of λ_i caused by the reduction of the boundary-layer thickness at the end of the base (due to the smaller λ_b) has a mild effect on OM1 side loads. As in the case of varying α, the base length does not have an important role in OM1 side-load duration. In fact, a 10% nonmonotonic variation of τ_{sl} is computed.

D. Influence of the Reynolds Number

The role of Reynolds number Re_c has been analyzed using the case of two lower values of Re_c with respect to the reference test case

Table 2 Geometric data of full-scale dual-bell nozzles for different values of the wall inflection angle α

λ_b	$Re_c \cdot 10^{-7}$	$\bar{M}_b$	$\bar{\gamma}_b$	α	$\pi_{\xi,e} \cdot 10^5$	$p_b/p_{\min}$	λ_i	τ_{sl}	$\Phi_{sl,max}$
16.60	1.04	4.45	1.265	13.68	3.0	3.66	3.81	0.439	0.31
16.60	1.04	4.45	1.265	17.62	3.0	4.84	4.13	0.482	0.26
16.60	1.04	4.45	1.265	23.07	3.0	7.52	4.26	0.442	0.18

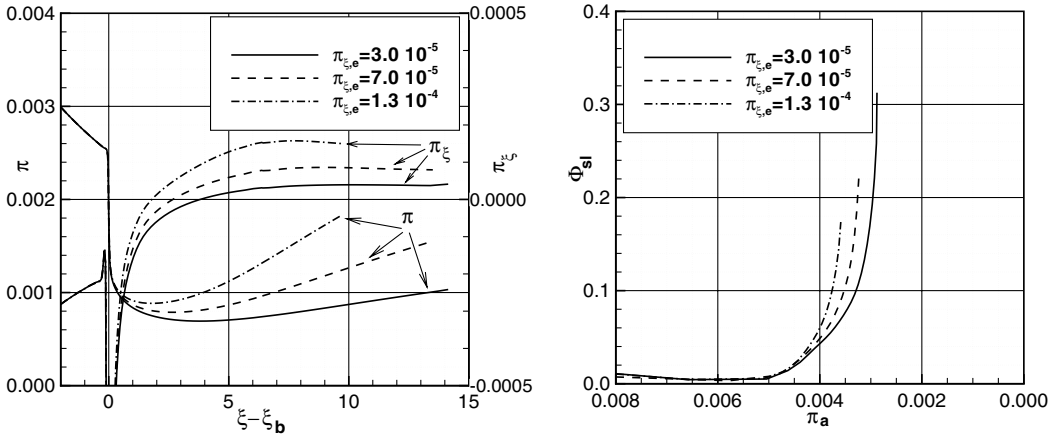

a) Wall pressure in the inflection region **b) Side loads for varying ambient pressure**

Fig. 6 Effect of the extension wall pressure gradient on the wall pressure behavior, inflection region length, and side loads.

reported on Table 1. The different Reynolds numbers can be easily obtained by considering different values of chamber pressure or throat radius. The results displayed in Fig. 8 show that the decrease of Re_c generates a smoother expansion at the inflection. As a consequence, the inflection region dimension increases and the average wall pressure gradient modulus in the inflection region decreases. The expected result, confirmed by Table 5, is that the side loads increase as Re_c decreases. In fact, there is an increase of both the maximum nondimensional side-load value and the range of altitude with high nondimensional side loads in the inflection region.

The results are shown in Fig. 8: the inflection region shrinks for increasing Re_c, but its width is not negligible, even in the case of the highest Re_c considered. For large Re_c, a quantitative evaluation of λ_i shows that it can still be as long as two times the nozzle throat diameter, although λ_i decreases in value, to zero, when approaching the inviscid flow. The final result is that both side-load parameters increase with decreasing Re_c, showing large strength and duration of side loads, especially in the case of the lowest Re_c.

E. Influence of Gas Properties

The influence of gas properties is studied here, focusing the attention on the role of γ, according to Eq. (12). The features of the inflection region obtained for the reference nozzle (full-scale nozzle operating with combustion gases) are compared with those of a subscale nozzle operating with cold gas (nitrogen). The subscale nozzle is made to show the same parameters of the reference nozzle, except for γ. Geometric and flow properties of the two nozzles are reported in Table 6 for the sake of clarity. Of course, a different gas yields a different behavior of the flowfield. In particular, it is evident that if Mach number similarity is prescribed, a different pressure behavior is obtained for a different γ. The selected subscale nozzle has a dimension 10 times smaller than the reference nozzle. The temperature is typical of subscale testing (i.e., 300 K), whereas the assigned pressure is chosen to provide the same value of Re_c as the reference nozzle. Although the behavior of computed wall pressure is quite different (Fig. 9), the simulations show that the inflection region of the two nozzles has similar dimension. Note that the nondimensional wall pressure in the subscale case is higher and the ratio of inflection to minimum wall pressure is larger. The comparison of the side-load intensity as a function of ambient pressure shows that although the curves are far from each other (the range of ambient pressures is wider in the case of $\gamma = 1.4$ and translated toward higher value of π_a), the two simulations show a nearly identical value of the maximum expected side load and only a 10% difference on critical time τ_{sl}. The computed values are reported in Table 7.

To confirm the preceding result, a second comparison of hot full-scale and cold subscale nozzle is carried out. The difference is that a shorter base ($\lambda_b = 12.17$) is considered, allowing a less uniform exit flow from the base and closer values of wall Mach number. Indeed, in the former case, the two nozzles show slightly different values of wall Mach number M_b. The computed behavior is quite similar to the previous comparison. The results reported in Table 7 again show close values for the inflection region dimension and, again, nearly the same value of nondimensional side-load maximum. As in the previous case, the larger difference appears in terms of nondimensional time with critical side loads, however, it is again in the 10% range.

F. Discussion

To conclude the study of the side-load behavior of the nozzle during OM1, some further consideration on the role of inflection and extension design should be made. To this goal, it is useful to remember that OM2 wall pressure behavior has to show a minimum to prevent the occurrence of operations with flow separation along the whole extension; therefore, only the positive pressure gradient is theoretically able to prevent this phenomenon [6]. A particular case is that of constant pressure extension ($\pi_{\xi,e} = 0$), in which the effect of the boundary layer is such to yield a behavior similar to the case of positive gradient extension. It has been shown in [6] that a constant pressure extension, with the same extension length and area ratio as the present LIP nozzle, indeed yields a minimum of pressure on the nozzle wall. However, the present analysis clearly shows increasingly critical side loads for decreasing the wall pressure gradient in the extension; thus, one could conject that the worst side-load performance would be for the case of constant pressure extension. Therefore, a large enough value of $\pi_{\xi,e}$ is required for a safer side-load behavior, whereas, on the contrary, the nozzle efficiency increases if the value of $\pi_{\xi,e}$ is reduced. The best choice of wall pressure gradient is, therefore, obtained by a trade-off between thrust efficiency and side loads during OM1.

The other parameters also affect both performance and side-load behavior. For instance, the value of α together with the value of $\pi_{\xi,e}$ determines the length of the second bell for the assigned expansion

Table 3 Geometric data of full-scale dual-bell nozzles for different values of the wall pressure gradient

λ_b	$Re_c \cdot 10^{-7}$	$\bar{M}_b$	$\bar{\gamma}_b$	α	$\pi_{\xi,e} \cdot 10^5$	$p_b/p_{\min}$	λ_i	τ_{sl}	$\Phi_{sl,\max}$
16.60	1.04	4.45	1.265	13.68	3.0	3.66	3.81	0.439	0.31
16.60	1.04	4.45	1.265	13.68	7.0	3.22	2.67	0.338	0.22
16.60	1.04	4.45	1.265	13.68	13.0	2.84	1.80	0.234	0.17

Table 4 Geometric data of full-scale dual-bell nozzles for different values of the base length λ_b

λ_b	$Re_c \cdot 10^{-7}$	$\bar{M}_b$	$\bar{\gamma}_b$	α	$\pi_{\xi,e} \cdot 10^5$	$p_b/p_{\min}$	λ_i	$\tau_{\rm sl}$	$\Phi_{\rm sl,max}$
16.60	1.04	4.45	1.265	13.68	3.0	3.66	3.81	0.439	0.31
14.38	1.04	4.45	1.265	13.68	3.0	3.72	3.40	0.402	0.25
12.17	1.04	4.45	1.265	13.68	3.0	3.81	2.99	0.443	0.24

ratio. Of course, this choice will affect divergence and friction losses and nozzle weight.

It is worth emphasizing that the length of the base (in other words, the shape of the base) is the parameter showing the smallest influence on the side-load intensity and duration.

Finally, important comparisons are those regarding nozzle scaling. The results show that the role of the Reynolds number on side loads is important and thus it has to be reproduced correctly in testing. Also, the nozzle operating gas (hot gas or cold gas) significantly affects the test in terms of wall pressure behavior. Nevertheless, if all the other parameters affecting the inflection region are the same, the effect of the gas on the nondimensional OM1 side-load parameters is almost negligible. In fact, if Reynolds number similarity is prescribed, cold subscale testing yields the same side-load intensity parameter, whereas the side-load duration parameter varies in the 10% range.

V. Transient Evolution from OM1 to OM2

When operation of a dual-bell nozzle passes from OM1 to OM2 because of the decrease of ambient pressure, the evolution of the flow in the extension, and thus the possible side loads, is governed by the design $\pi_{\xi,e}$, by the properties of the inflection region, and by the rate of variation of the pressure ratio. For this reason, the behavior of the nozzle flow during transition from OM1 to OM2 is studied by simulating different test cases featuring different chamber pressure variations in time and different nozzle Reynolds numbers. Indeed, it has been shown in the foregoing section that the inflection region is quite sensitive to the Reynolds number; thus, the study of the role of the Reynolds number on the OM1–OM2 transition is a significant test to evaluate the more general effect of the different parameters of Sec. IV.

Time-accurate axisymmetric simulations of transition have been carried out by enforcing a little and slow variation of chamber pressure, starting from a steady-state OM1 solution with the separation point located nearly at the end of the inflection region. Chamber temperature is held constant during the whole simulation. The reference nozzle in this case is a cold-flow subscale nozzle having the properties summarized in Table 8. The nondimensionalization of variables is made, choosing a reference time of a value based on the chamber speed of sound a_c and the reference length. The nondimensional time is, therefore, $\tau = t/(r_t/a_c)$. Moreover, the initial chamber pressure value $p_{c,0}$ has been chosen as the reference pressure value and the nozzle $Re_{c,0}$ evaluated accordingly. Velocity

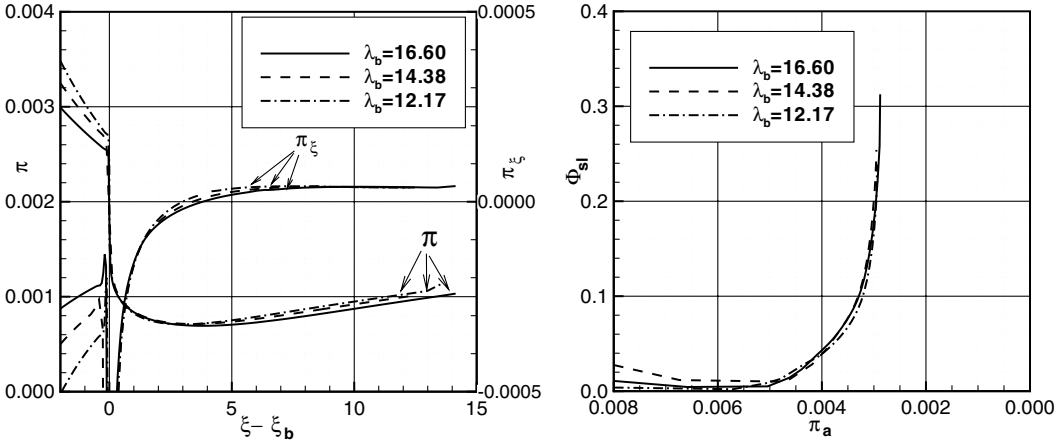

a) Wall pressure in the inflection region b) Side loads for varying ambient pressure

Fig. 7 Effect of the base length on the wall pressure behavior, inflection region length, and side loads.

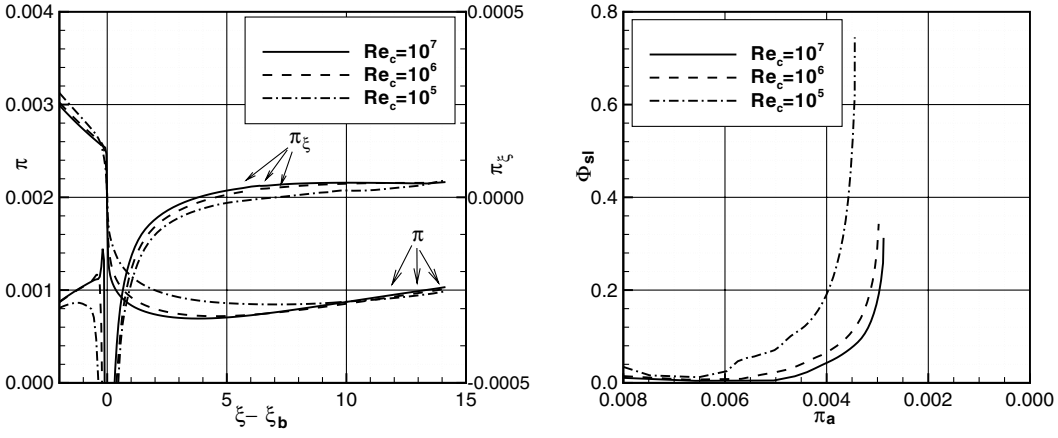

a) Wall pressure in the inflection region b) Side loads for varying ambient pressure

Fig. 8 Effect of the Reynolds number on the wall pressure behavior, inflection region length, and side loads.

Table 5 Summary of main features of the inflection region at varying Reynolds numbers

λ_b	$Re_c \cdot 10^{-7}$	$\bar{M}_b$	$\bar{\gamma}_b$	α	$\pi_{\xi,e} \cdot 10^5$	$p_b/p_{\min}$	λ_i	$\tau_{\rm sl}$	$\Phi_{\rm sl,max}$
16.60	1.04	4.45	1.265	13.68	3.0	3.66	3.81	0.439	0.31
16.60	0.10	4.45	1.265	13.68	3.0	3.59	4.54	0.550	0.34
16.60	0.01	4.45	1.265	13.68	3.0	3.07	7.07	0.585	0.74

Table 6 Geometric and combustion chamber data of the hot full-scale and the cold subscale dual-bell nozzle

	Full scale, LOX/LH2	Subscale, N2
Throat radius r_t, m	0.1	0.01
Chamber temperature T_c, K	3500	300
Chamber pressure p_c, MPa	12.0	4.9
Nondimensional base length λ_b	16.60	16.60
Nondimensional extension length λ_e	14.30	6.45
Nondimensional divergent section length λ_o	30.90	23.05
Base area ratio ϵ_b	48.0	15.9
Overall area ratio ϵ_o	115	29.4
Oxidizer to fuel mass ratio O/F	6	-
Average (1-D) Mach number at base exit $\bar{M}_b$	4.45	4.45
Ratio of specific heats γ_c, $\bar{\gamma}_b$	1.19, 1.26	1.40
Inflection angle α	13.68 deg	13.68 deg
Chamber Reynolds number $Re_c = \rho_c a_c r_t/\mu_c$	10^7	10^7
Nondimensional wall pressure gradient, extension design $\pi_{\xi,e}$	$3 \cdot 10^{-5}$	$3 \cdot 10^{-5}$

and acceleration are nondimensionalized, choosing as reference values the chamber speed of sound a_c and the ratio a_c^2/r_t, respectively.

The typical time evolution of wall pressure is shown in Fig. 10, in which the plots are relevant to a sequence featuring a constant time interval $\Delta\tau = 18$. The separation point moves from left to right, and it can be seen that the distance between each pair of curves increases up to a maximum, and then it decreases, indicating an acceleration followed by a deceleration. The last two curves are close to each other, showing a strong reduction of separation-point velocity. The evolution of the separated flow region is summarized in Fig. 11, in which the position ξ_s, velocity $\dot{\xi}_s$, and acceleration $\ddot{\xi}_s$ of the separation point in time are superimposed to the plot of OM2 wall pressure and of its gradient. Note that the separation-point abscissa has been chosen as an independent variable axis to emphasize the behavior of velocity and acceleration of the separation point as a function of its position in the extension. Time is assumed to be $\tau = 0$ when the separation point starts moving. Figure 11 more clearly confirms the behavior presented in Fig. 10; the separation point moves slowly at the beginning, when it lies in the region of pressure minimum, then it accelerates, reaching a nearly constant value of acceleration and, accordingly, an increasing value of velocity. Finally, near a certain abscissa, it slows down again. According to the different features of the separation-point movement, three different subregions can be identified: an acceleration region, a transition region in which it moves fast, and a deceleration region close to the nozzle end. The width of these subregions depends on the particular case considered. Here, the attention is focused on the behavior of the separation point in the transition region, which covers most of the extension. To make easier the comparison of the separation-point evolution for all the computations performed, a common transition region has been identified as the region going from $\xi = 10$ to $\xi = 15.5$, and shown in Fig. 12, in which the origin of the time axis is at the entrance of the separation point in the common transition region.

The behavior of the separation point in the acceleration and deceleration region is not considered here, because it depends on parameters different from the geometry of the extension. This is clear for the acceleration region, in which a role is played by the exact initial position of the separation point (it will never be placed exactly at the end of the inflection region) and by its velocity at the exit of the inflection region, which depends on the chamber pressure variation rate and, again, on the exact initial position of the separation point. Less clear is the behavior of the separation point in the deceleration region, in the vicinity of the nozzle tip. The deceleration is not justified by the wall pressure gradient that is nearly the same as in the transition region. Nevertheless, the existence of such a deceleration has been shown to also take place in the case of higher positive wall pressure gradients. The studies carried out on different extension profiles [6] indicate that the movement of the separation point near

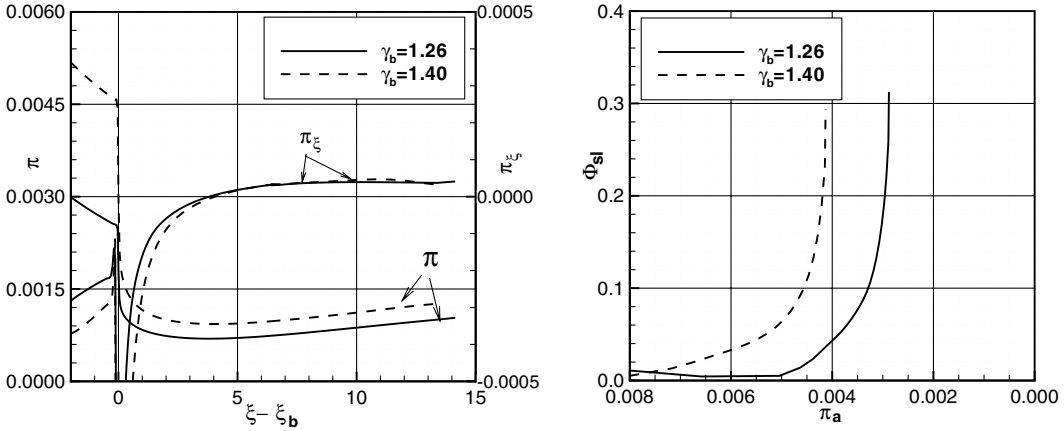

a) Wall pressure in the inflection region **b) Side loads for varying ambient pressure**

Fig. 9 Effect of the γ on the wall pressure behavior, inflection region length, and side loads.

Table 7 Summary of main features of the inflection region at varying γ

λ_b	$Re_c \cdot 10^{-7}$	$\bar{M}_b$	$\bar{\gamma}_b$	α	$\pi_{\xi,e} \cdot 10^5$	$p_b/p_{\min}$	λ_i	τ_{sl}	$\Phi_{sl,max}$
16.60	1.04	4.45	1.265	13.68	3.0	3.66	3.81	0.439	0.31
16.60	1.04	4.45	1.400	13.68	3.0	4.91	4.06	0.491	0.29
12.17	1.04	4.45	1.265	13.68	3.0	3.81	2.99	0.443	0.24
12.17	1.04	4.36	1.400	13.68	3.0	4.81	3.29	0.407	0.25

Table 8 Geometric data and combustion chamber operating conditions of the dual-bell nozzle considered for transient simulations

Throat radius r_t, m	0.01
Chamber temperature T_c, K	300
Chamber pressure $p_{c,0}$, MPa	1.74
Nondimensional base length λ_b	7.4
Nondimensional extension length λ_e	9.6
Nondimensional divergent section length λ_o	17.0
Base area ratio ϵ_b	13.56
Overall area ratio ϵ_o	38.65
Average (1-D) Mach number at base exit $\bar{M}_b$	4.267
Ratio of specific heats γ_c, $\bar{\gamma}_b$	1.4
Inflection angle α	12.16 deg
Chamber Reynolds number $Re_{c,0} = \rho_{c,0} a_c r_t/\mu_c$	$3.7 \cdot 10^6$
Nondimensional wall pressure gradient, extension design $\pi_{\xi,e}$	$1.6 \cdot 10^{-4}$

the end of the nozzle cannot be considered as mainly depending on $\pi_{\xi,e}$. In the following sections, a comparative analysis is presented of the influence of some of the most important parameters on the nozzle behavior during transition. In particular, their effect on the transition time τ_{tr} is discussed; τ_{tr} is defined as the time required for the separation point to cross the transition region λ_{tr}.

A. Effect of Chamber Pressure Ramping on Transition Time

The separation point moves downstream as chamber pressure increases. Of course, there will be a delay from the instant when chamber pressure starts changing to the instant when the separation point starts moving. Moreover, if the driving force for the movement of the separation point is the pressure difference between the initial and present pressure values, the velocity of displacement of the separation point is expected to change according to the rate of change of the chamber pressure. This is an important dependence, however, it is more related to the engine throttling or to the vehicle trajectory (i.e., ambient pressure variation rate) than to the nozzle geometry. Therefore, to emphasize the role of the nozzle geometry on the transition behavior, an analysis has been carried out implementing sufficiently slow and small chamber pressure rampings to yield almost no dependence on chamber pressure variation rate. In particular, chamber pressure rampings are such that the final value of PR is reached in the chamber before the separation point has moved from the inflection region.

To confirm that the results are independent of chamber pressure ramping, three different cases have been considered. Each case, carried out at constant ambient pressure, can be identified by the rate of change of the nozzle pressure ratio $\dot{PR} = dPR/d\tau$, for which the value has been changed by orders of magnitude (from $\sim 10^{-3}$ up to ~ 1). This comparison has been carried out at $Re = 3.7 \cdot 10^6$, with PR going from 121.5 to 122 ($\Delta PR = 0.5$). Again, to make the comparison easier, time has been considered zero when the separation point enters the transition region. Figure 13 shows that there are only slight differences, originated by the different velocity of separation point at the transition region entrance. However, the behavior of the separation-point velocity and acceleration are quite similar. The consequence is that the transition time remains unchanged over the range of variation of chamber pressure ramping implemented. This result is summarized in Table 9, in which the computed values of transition times are reported. They indicate that within the present range of $\dot{PR}$ and for the values of ΔPR and $Re_{c,0}$ considered, transition time is only dependent on nozzle geometry,

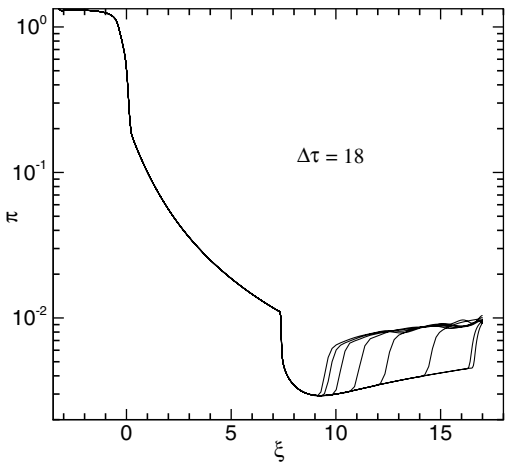

Fig. 10 Wall pressure evolution during transition.

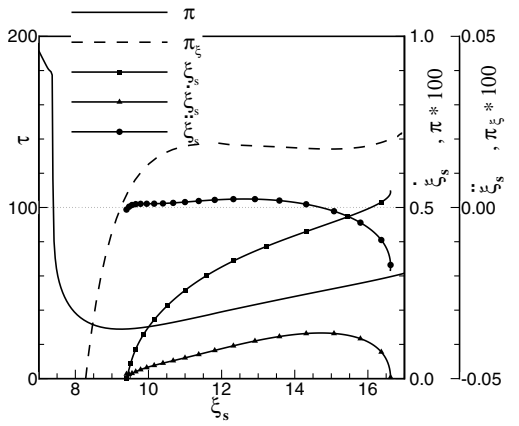

Fig. 11 Evolution of separation-point position, velocity, and acceleration during transition.

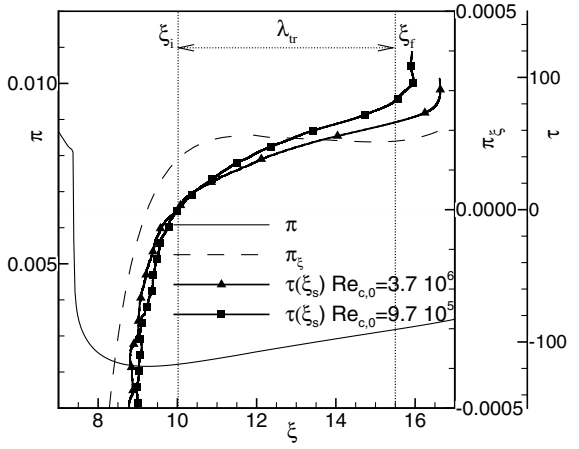

Fig. 12 Common transition region λ_{tr} compared with the evolution of the separation-point position at different Reynolds numbers and with a typical OM2 wall pressure behavior.

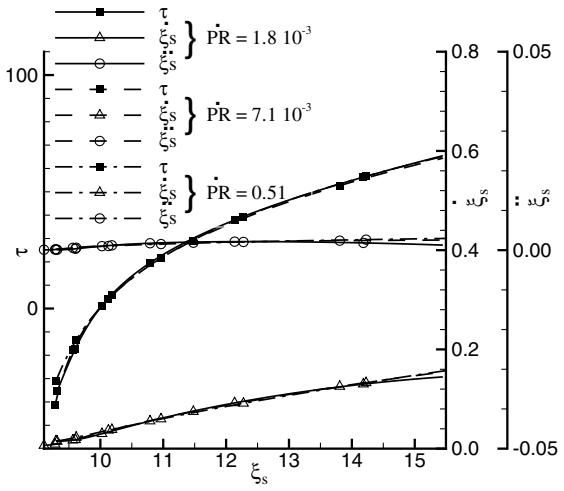

Fig. 13 Comparison of separation-point position, velocity, and acceleration during transition for different values of chamber pressure ramping.

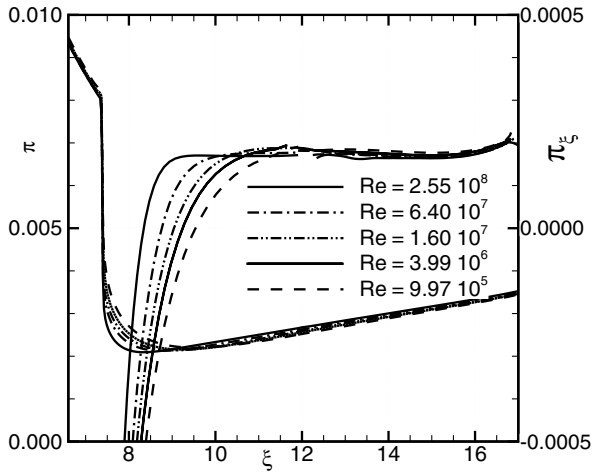

Fig. 14 Wall pressure and wall pressure gradient at the inflection region for varying Re_c.

whereas it is independent of chamber pressure ramping. For this reason, only chamber pressure rampings with small ΔPR are considered in the following, which exclude any effect of $\dot{PR}$ on the present analysis. If larger values of ΔPR were considered, the continuously increasing chamber pressure might affect the separation-point evolution. For instance, for the case with $\dot{PR} = 7.1 \cdot 10^{-3}$, the transition time is slightly reduced when $\Delta PR = 1.5$ and the final PR is 123 ($\tau_{tr} = 63$); however, further increasing the final value of PR no longer affects the transition time. The reason for this behavior can be easily understood if one considers that if $\tau_{tr} = 63$ and $\dot{PR} = 7.1 \cdot 10^{-3}$, during this "fast" transition, the pressure ratio change is $\Delta PR = 0.45$. Further increase of ΔPR will take effect on the separation point only after it has moved beyond the transition region. The conclusion is that if $\dot{PR}$ is small enough, there is no effect on the computed transition time, which is therefore a characteristic transition time of the considered geometry.

As a final remark, the values of $\dot{PR}$ considered previously should be compared with the practical values. Typical values are $\dot{PR} \sim 4.6 \cdot 10^{-3}$ for a Vulcain engine startup [19], $\dot{PR} \sim 6.0 \cdot 10^{-4}$ for an Ariane 5 launch trajectory [9], and $\dot{PR} \sim 1.4 - 5.6 \cdot 10^{-5}$ for a subscale test of [4]. Therefore, the present range of $\dot{PR}$ includes values far larger than those that can be practically expected, thus indicating that there is no effect of chamber pressure ramping rate on transition time in practical applications.

The preceding discussion is not in contradiction with the necessity or the advantage of chamber pressure throttling to improve dual-bell nozzle transition properties. In fact, throttling can reduce the time of OM1 operations with the separation point in the inflection region.

B. Effect of Nozzle Reynolds Number on Transition Time

The foregoing section has shown that in steady-state conditions, the length of the inflection region (and thus the effective nozzle geometry) depends on the nozzle Reynolds number, and that may yield some slight differences between subscale and large-scale nozzles. A second aspect to be investigated is the time evolution of the separated flow region during transition from OM1 to OM2. To this end, three different simulations of transition have been carried out, all featuring a chamber pressure ramping rate of $\dot{PR} = 7.1 \cdot 10^{-3}$, and each with a different value of $Re_{c,0}$. The differences in the inflection region for varying Re_c are shown in Fig. 14 by the OM2 wall pressure behavior in the extension.

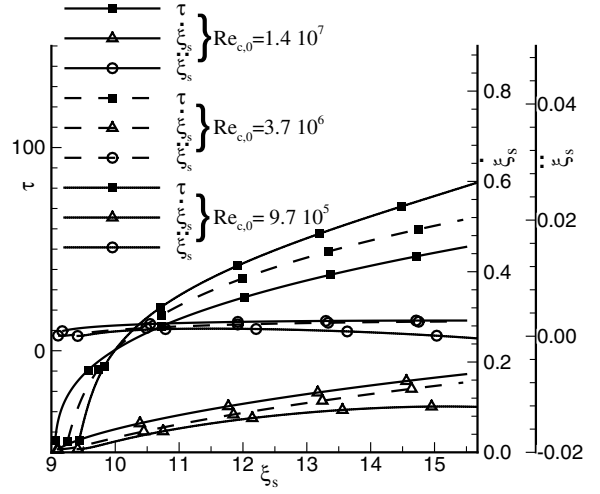

Fig. 15 Comparison of separation-point position, velocity, and acceleration during transition for different values of nozzle Reynolds numbers.

The nozzle behavior during transition is summarized by Fig. 15, in which position, velocity, and acceleration of the separation point in the transition region are plotted as functions of time. Once again, time has been set to zero as the separation point enters the transition region. Figure 15 shows that the changes of the effective geometry induced by the different boundary-layer thickness yield appreciable differences of the separation-point evolution. In particular, it can be seen that the separation-point velocity increases with increasing $Re_{c,0}$. For instance, at $Re_{c,0} = 1.4 \cdot 10^7$, the separation point reaches the location $\xi = 13$ in nearly half the time than at $Re_{c,0} = 9.7 \cdot 10^5$. This is mainly due to the fact that as $Re_{c,0}$ increases, λ_i decreases and the positive pressure gradient region enlarges, which means that the region in which the separation point accelerates also enlarges. It is interesting to note that except for the lowest Reynolds number considered, the separation-point acceleration seems to be a function of the wall pressure gradient: a constant value is reached in the constant gradient region. The behavior of the separation-point abscissa as a function of time in Fig. 15 clearly shows that the

Table 9 Comparison of the transition time for various chamber pressure rampings

$\dot{PR}$	$1.8 \cdot 10^{-3}$	$7.1 \cdot 10^{-3}$	0.51
τ_{tr}	65	66	65

Table 10 Comparison of the transition time for different values of nozzle Reynolds numbers.

$Re_{c,0}$	$9.7 \cdot 10^5$	$3.7 \cdot 10^6$	$1.4 \cdot 10^7$
τ_{tr}	82	66	50

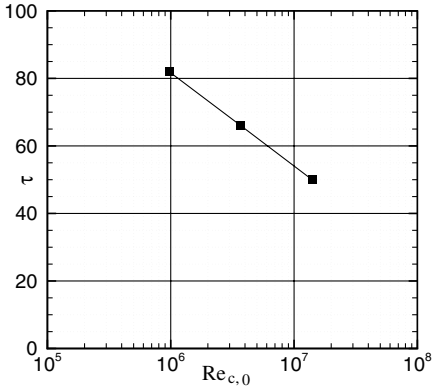

Fig. 16 Evolution of transition time for varying Reynolds numbers.

transition time decreases for increasing $Re_{c,0}$. The monotonic reduction of transition time for increasing $Re_{c,0}$ can be better seen in Table 10 and also in Fig. 16. Increasing $Re_{c,0}$ by a factor of 14 yields a 40% reduction of τ_{tr}. This indication is meaningful when trying to extrapolate results from experimental tests to nozzles of different scale. Pure geometrical scaling of transition time between nozzles having the same shape, propulsion gas, and chamber temperature is therefore only possible in the case of nozzles having the same Reynolds number. It is interesting to note that the dimensional transition time is rather short. For instance, in the case of the reference nozzle (Table 8), the dimensional transition time is $t_{tr} = 1.87$ ms.

VI. Conclusions

It has been shown with a simple model that the separation point could spend as long as several seconds in the most critical part of the inflection region during the ascent of the launcher. Because the properties of the inflection region have been found to be key parameters in quantifying the expected side loads, the design parameters affecting this region have been identified and their effect analyzed. These parameters are the boundary-layer thicknesses at the end of the base, the Prandtl–Meyer expansion at the inflection, and the wall pressure gradient of the extension. It has been found that there is a trade-off between thrust efficiency and side-load performance, and the design choice of parameters such as inflection angle or extension wall pressure gradient may significantly change the intensity and duration of side loads acting in the proximity of the wall discontinuity in the first phase of the flight. The identification of the main parameters affecting the inflection region has also indicated the theoretical aerodynamics scaling of the inflection region from a cold subscale model to a hot full-scale application. Only by reproducing all the parameters can the nondimensional side-load behavior be correctly evaluated. Nevertheless, the gas properties have a negligible effect on side-load intensity and yield a small change of side-load duration. As a consequence, subscale cold testing can still be useful, provided that the similarity is preserved for all the other parameters (inflection angle, extension wall pressure gradient, nozzle Reynolds number, base length, and base exit Mach number).

The analysis of the transition toward the high-altitude operating mode has shown that the transition time is independent of chamber pressure ramping, provided that the variation of chamber or ambient pressure is sufficiently slow. The consideration that this value is actually slow in practical cases has to be kept in mind when aiming to predict the transition behavior of full-scale nozzles by subscale cold testing. The analysis of transition for varying Reynolds numbers has also emphasized the role of the inflection region on the evolution of the separation point along the extension. The result is that the conclusions made for the evaluation of nozzle side loads in the low-altitude operating mode can also be extended to the case of evaluation of transition side loads: only reproducing all parameters affecting the flow behavior in the inflection region permits a correct prediction of dual-bell nozzle side-load intensity and duration.

Acknowledgments

The present study has been carried out in the framework of programs ESA/ESTEC-TRP, ESTEC Contract No. 15575/01/NL/CK and ESA/ESTEC-GSTP, ESTEC Contract No. 16301/02/NL/SFc. Funding from the Italian Ministry of Scientific and Technological Research (MIUR) is also acknowledged.

References

[1] Horn, M., and Fisher, S., "Dual-Bell Altitude Compensating Nozzle," NASA CR-194719, 1994.

[2] Hagemann, G., Immich, H., Nguyen, T. V., and Dumnov, G. E., "Advanced Rocket Nozzles," *Journal of Propulsion and Power*, Vol. 14, No. 5, Sept.–Oct. 1998, pp. 620–634.

[3] Perego, D., and Schwane, R., "Simulation od Unsteady Three Dimensional Separation Behaviour in Truncated Ideal Contour Nozzle," 40th AIAA/ASME/SAE/ASEE Joint Propulsion Conference, AIAA Paper 2004-4015, July 2004.

[4] Hagemann, G., Terhardt, M., Haeseler, D., and Frey, M., "Experimental and Analytical Design Verification of the Dual-Bell Concept," *Journal of Propulsion and Power*, Vol. 18, No. 1, Jan.–Feb. 2002, pp. 116–122.

[5] Hieu Le, T., Girard, S., and Alziary de Roquefort, T., "Direct Measurement of Side Loads with Transonic Buffeting," Proceedings of the Fifth European Symposium on Aerothermodynamics for Space Vehicles, Cologne, Germany, 2004 ESA/European Space Research and Technology Centre (ESTEC), Paper SP-563, Noordwijk, South Holland, The Netherlands, 2005.

[6] Nasuti, F., Onofri, M., and Martelli, E., "Role of Wall Shape on the Transition in Axisymmetric Dual-Bell Nozzles," *Journal of Propulsion and Power*, Vol. 21, No. 2, Mar.–Apr. 2005, pp. 243–250.

[7] Schmucker, R. H., "Flow Process in Overexpanded Chemical Rocket Nozzles, Part 2: Side Loads Due to Asymmetric Separation," NASA TM-77395, Feb. 1984.

[8] Immich, H., and Caporicci, M., "Status of the FESTIP Rocket Propulsion Technology Programme," 33rd AIAA/ASME/SAE/ASEE Joint Propulsion Conference, AIAA Paper 97-3311, July 1997.

[9] Hagemann, G., Frey, M., and Manski, D., "A Critical Assessment of Dual-Bell Nozzles," 33rd AIAA/ASME/SAE/ASEE Joint Propulsion Conference & Exhibit, AIAA Paper 97-3299, July 1997.

[10] Schmucker, R. H., "Flow Process in Overexpanded Chemical Rocket Nozzles, Part 1: Flow Separation," NASA TM-77396, Jan. 1984.

[11] Schlichting, H., *Boundary Layer Theory*, Pergamon, London, 1955.

[12] Bartz, D., "An Approximate Form of Compressible Turbulent Boundary Layer Development in Convergent-Divergent Nozzles," *Transactions of the ASME*, Vol. 77, 1955, pp. 1235–1245.

[13] Nasuti, F., and Onofri, M., "Analysis of Unsteady Supersonic Viscous Flows by a Shock Fitting Technique," *AIAA Journal*, Vol. 34, No. 7, July 1996, pp. 1428–1434; also AIAA Paper 95-2159.

[14] Nasuti, F., "A Multi-Block Shock-Fitting Technique to Solve Steady and Unsteady Compressible Flows," *Computational Fluid Dynamics 2002*, edited by S. Armfield, P. Morgan, and K. Srinivas, Springer–Verlag, Berlin, 2003, pp. 217–222.

[15] Moretti, G., "A Technique for Integrating Two-Dimensional Euler Equations," *Computers and Fluids*, Vol. 15, No. 1, 1987, pp. 59–75.

[16] Martelli, E., "Studio Della Fluidodinamica Interna di Ugelli Propulsivi di Tipo Dual Bell," Ph.D. Thesis, Dept. of Mechanics and Aeronautics, Univ. of Rome "La Sapienza," Rome, Italy, 2005 (in Italian).

[17] Paciorri, R., and Sabetta, F., "Compressibility Correction for the Spalart-Allmaras Model in Free-Shear Flows," *Journal of Spacecraft and Rockets*, Vol. 40, No. 3, May 2003, pp. 326–331.

[18] Spalart, P. R., and Allmaras, S. R., "A One-Equation Turbulence Model for Aerodynamic Flows," *La Recherche Aerospatiale: Bulletin Bimestriel de L'office National D'etudes et de Recherches Aerospatiales*, No. 1, 1994, pp. 5–21.

[19] Caporicci, M., Eriksson, L. E., Pekkari, L. O., Onofri, M., Popp, M., and Weiland, C., "Advanced Nozzle Technologies for the Ariane 5 Vulcain Engine," 30th AIAA/ASME/SAE/ASEE Joint Propulsion Conference, AIAA Paper 94-3263, June 1994.

[20] Martelli, E., Nasuti, F., and Onofri, M., "Size Effects on the Transition in Dual Bell Nozzles," 40th AIAA/ASME/SAE/ASEE Joint Propulsion Conference, AIAA Paper 2004-3999, July 2004.

T. Jackson
Associate Editor